EGTRIB Journal
JOURNAL OF
THE EGYPTIAN SOCIETY OF TRIBOLOGY
VOLUME 22, No. 2, April 2025, pp. 80 - 90 ISSN 2090 - 5882
(Received January 29. 2025, Accepted in final form March 25. 2025) jest.journals.ekb.eg

IMPROVING THE CONTROL SYSTEMS FOR DESERT MINERAL EXPLORATION ROVERS AND MODELING OF FRICTION AND SLIP

Amr E. Rafaat and Ezzat A. A.

Mechatronics Engineering Department, Higher Institute of Engineering and Technology,
New Minia, EGYPT.

ABSTRACT
Exploration rovers are the optimal solutions for a well-structured environment like roads or flat and regular terrain. In the present work, A smart control system that helps the rover adjust its wheel motion in real-time depending on how much it is slipping is discussed. The friction and slip for desert mineral exploration rovers wheels was investigated. Slip and velocity and their effect on friction were investigated. The friction coefficient values obtained from previous documented experimental results are used as input data for the simulation model to achieve the same properties. Based on the results, it was found that the proposed friction model and control system improves the rover's performance and makes it more reliable for such tasks. The rover keeps good traction, saves energy, and stays stable while moving. The need of autonomous robots that can move efficiently and safely in difficult environments.

KEYWORDS
Rover control system, Exploration rover, Friction modeling, Slip dynamics.

INTRODUCTION
For missions in isolated, dangerous, and unstructured areas-like the Earth's deserts and planetary surfaces—exploration rovers are crucial. Traditional movement tactics frequently fail in sand-filled, uneven terrains encountered by rovers in terrestrial applications such as mineral prospecting. Accurately simulating the interaction between wheels and dirt is essential for successful navigation, especially in situations with slip and fluctuating friction. The mobility and energy efficiency of a rover are directly impacted by friction and slide. A wheel loses traction when it slips longitudinally or laterally, which can limit forward motion, raise power consumption, and eventually put the wheel at risk of immobilization. Therefore, enhancing rover autonomy and dependability requires both accurate friction modeling and adaptive control systems.

Wong and Reece's early work established the fundamentals of terramechanics, while Ishigami et al. expanded on these ideas by adding experimentally verified slip dynamics, [1]. In order to improve mobility over loose terrains, real-time adaptation and sensor fusion have been the focus of more recent research, [2]. To limit wheel slip when navigating across granular soils, for example, Zhang et al. suggested a terrain-adaptive control technique that integrates proprioceptive and exteroceptive sensing, [3]. In a similar vein, Zhang and Wang created a physics-informed neural network (PINN)

model that achieved good accuracy while requiring less computing power to forecast wheel-soil interaction forces, [4].

Slip estimation using data-driven modeling and machine learning has been investigated in other recent works. In order to improve control performance in changeable desert conditions, Li et al. introduced a hybrid model that combines neural networks with analytical Terr mechanics equations to forecast wheel slide in real-time. Furthermore, friction testing equipment is still essential for computing these models, [5]. In a recent study, for instance, Kumar et al. used a mobile friction tester to gather soil-traction data from several desert locations, which they then fed into modeling tools to optimize rover operation, [6].

Few studies directly integrate field-based testing, friction modeling, and real-time control specifically designed for mineral exploration, despite these advancements. A slip-aware friction model based on both longitudinal and lateral dynamics, experimental validation using a friction tester in a desert environment, and an adaptive control system that modifies steering and wheel torque in real time are the three integrated solutions presented in this paper to close that gap. This strategy is intended to increase the rover's operating effectiveness and terrain flexibility, particularly for autonomous mineral prospecting missions.

Methodology

Exploration Rovers

The six-wheeled "Exploration Rover" has a very light aluminum body. In order to fit the electrical box, batteries, rover hand, and other components, the frame is created to attach many plastic boxes without covers. The primary body of the rover measures 35"x21"x10", while the entire rover measures 60"45"x22".

Table 1 List of components weight.

No.	Name of components	Weight	No of items	Total weight
1.	Rover chassis	5	1	5
2.	Joint servo mount 1	0.250	2	0.5
3.	Joint servo mount 2	0.250	2	0.5
4.	Main joint	0.750	2	1.5
5.	Rocker joint	2	2	4
6.	Bogie joint 1	0.350	2	0.7
7.	Bogie joint 2	0.2	2	0.4
8.	Wheel joint	1.5	4	6
9.	Wheels	0.25	8	2
10.	Differential bar	3	1	3
ER Total weight				23.6
All weight in kilograms				

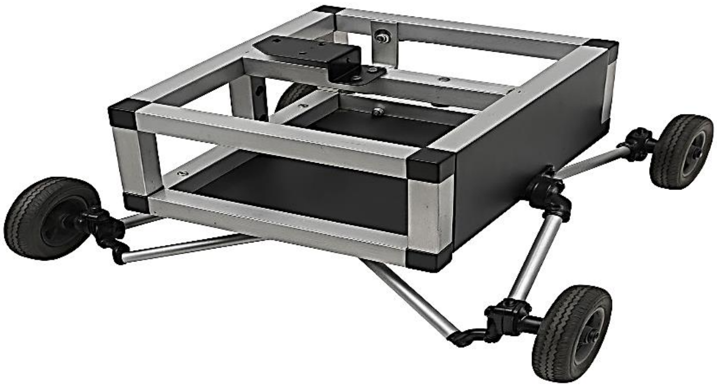

Fig. 1 Desert Mineral Exploration Rovers.

Material Selection

Because a heavier mobile robot requires more power to operate, it will need a larger actuator and a battery with a larger capacity. Because aluminum alloy is lighter than steel and other metals, it was first taken into consideration. As a result, aluminum alloy is chosen as the structural material.

Table 2 Examples of stress analysis for parts of exploration rovers.

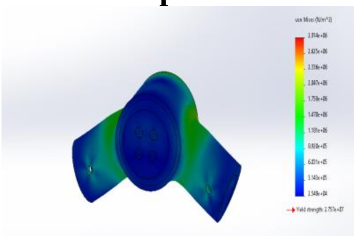	**Main joint**	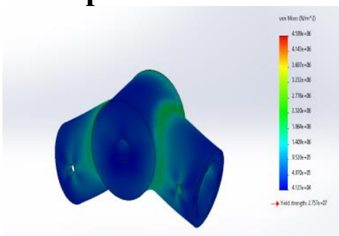	**Bogie joint 1**
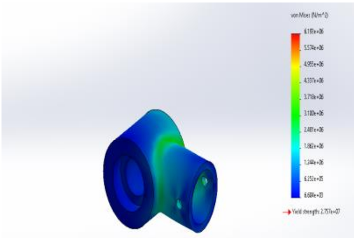	**Bogie joint 2**	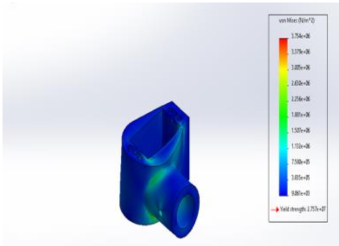	**Joint servo mount 1**
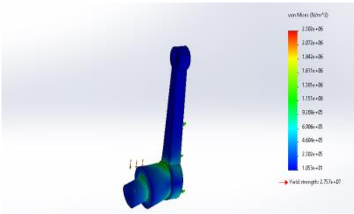	**Rocker joint**	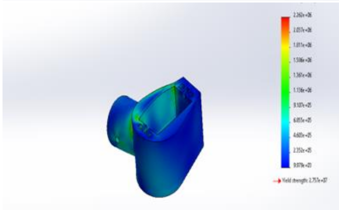	**Joint servo mount 2**

Rover control system

The rover's mobility is managed by the motion control system using an Arduino and Raspberry Pi. The Raspberry Pi is served by a Python software, while the control station is a client running another Python program. The UDP protocol is used to communicate between clients and servers. The four primary control signals for the rover are UP, DOWN, LEFT, and RIGHT. There are extra signals for GEAR and POWER. Up to four gears, each twice as fast as the one before it, can be designated by the control system. Since the Raspberry Pi is unable to supply PWM6 signals, it gets the signal from the control station and sends it to the Arduino.

Similar to a D/A converter, the Arduino transforms the Raspberry Pi's digital signal into an analog form before sending it to the motor driver. According to our program, each level of signal voltage indicates the rover's direction and speed of motion: 2.5V for a steady state, 5V for full speed forward, and 0V for full speed reverse motion. The control station has complete control over the rover thanks to three duals connected to six motors. Five motor drivers and a Raspberry Pi make up the hand control system, which is managed by digital signals. The Raspberry Pi runs a Python server software, while the control station runs a Python client program that uses the UDP protocol.

Base, Shoulder, Arm, Wrist, and Claw are the five fundamental parts that can be operated from the control station. The power sources for the actuators and motors have been determined based on the output that the Raspberry Pi's GPIO7 pins provide in response to the signal. It is possible to control several hand parts at once. A one-second disconnection safety process is also included in this system. The program gets the rover's location from the satellite and relays it to the GPS sensor. The compass sensor provides the rover's north angle. Two sensors provide information that is utilized to determine whether the rover has arrived at its target and to choose the best course of action for it.

To obtain the data we need, the two sensors are combined with an Arduino Uno and communicated to the server program. One of the key components of our navigation system is an RPLIDAR device. It helped with navigation chores and was utilized for 2D mapping. We can obtain the coordinates of the rover's present location via the GPS system. We mapped our surroundings and located roadblocks using RPLIDAR. We can get up to 2000 samples from it every second. The RPLIDAR device uses lasers with a 6 m range and 3600 scanning. It primarily employs lasers to identify environmental impediments, and we have utilized Java software for mapping.

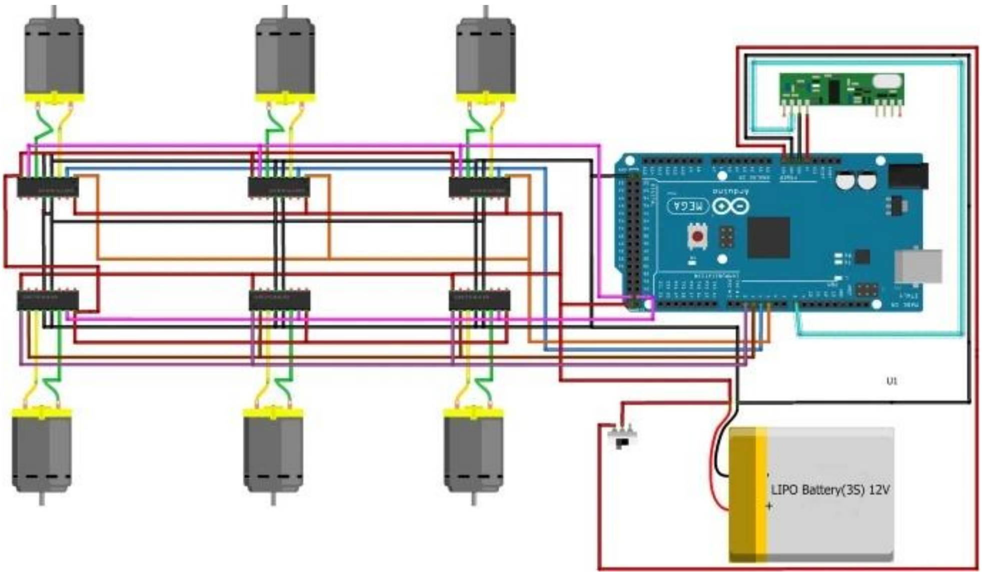

Fig. 2 control system of rover.

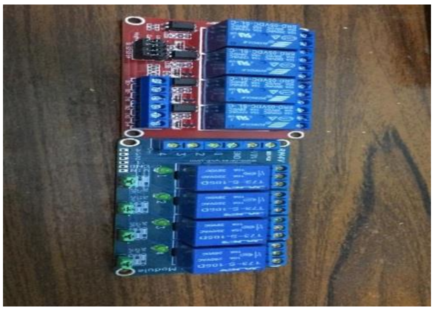

DC motor (24 v): **Relay's:**

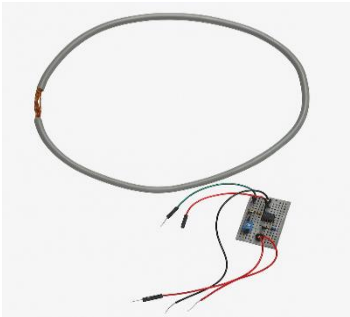

Metal sensor detector **Raspberry Pi:**

Fig. 3 Examples of control system components.

Friction Modeling

When there is a relative velocity between the tyre contact point and the driving surface, all force produced by the rover's wheels results from the interaction between the tyre and the surface, [7]. Thus, both propulsive and resistive forces originate from friction. The friction model uses the wheel's rotating velocity, ω, which is provided by the motor model.

Figure 3 shows the velocity components generated within the model, where u_{wc} and v_{wc} are the surge and sway velocities of the wheel center point, respectively. Therefore, $\vec{v}_{wc}$ is the resultant velocity of the wheel center is rotated from the surge axis by the sideslip angle of the wheel, α. The friction model requires an accurate calculation of the tangential velocity of the tyre at the contact point between the wheel and the ground, u_{tan}. In Fig. 1, u_{wc} is greater than u_{tan}, therefore the wheel is rotating slower than its translational motion, and the rover is braking.

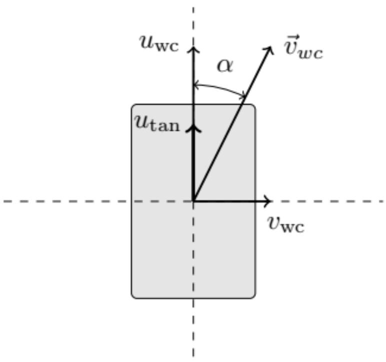

Fig. 4 Velocity components resulting from the interaction of the driving surface and the rover wheel.

Vertical Wheel Forces

As the rover experiences longitudinal and lateral accelerations, the vertical forces applied to each of the rover wheels vary. Vertical wheel forces F_{ZT} for each one of the four wheels are distributed as in Equation (1).

$$F_{ZT} = m.g.\cos(\theta).\cos(\phi)[K_1 \quad K_2 \quad K_3 \quad K_4]^T \tag{1}$$

where m is the mass of the rover, g is the gravitational acceleration, θ and ϕ are pitch and roll angles, and K_n is the weight distribution ratio for each wheel and is calculated using Equations (2) and (3).

$$\begin{aligned} K_1 &= K_{front}K_{left} \\ K_2 &= K_{rear}K_{left} \\ K_1 &= K_{front}K_{right} \\ K_1 &= K_{rear}K_{left} \end{aligned} \tag{2}$$

$$\begin{aligned} K_{front} &= \frac{l_r}{L} - \frac{h}{L}\left(\tan(\theta) + \frac{a_X}{g.\cos(\theta)}\right) \\ K_{rear} &= \frac{l_f}{L} + \frac{h}{L}\left(\tan(\theta) + \frac{a_X}{g.\cos(\theta)}\right) \\ K_{left} &= \frac{1}{2} - \frac{h}{L}\left(\tan(\phi) + \frac{a_Y}{g.\cos(\phi)}\right) \\ K_{right} &= \frac{1}{2} + \frac{h}{L}\left(\tan(\phi) + \frac{a_Y}{g.\cos(\phi)}\right) \end{aligned} \tag{3}$$

where h is the height of centre of gravity of the rover, w is the width of the rover, a_X the longitudinal acceleration, a_Y the lateral acceleration, and l_r and l_f are the rear and front moment arm, $L = l_r + l_f$.

Wheel Centre Velocity

The rover's surge, sway, and yaw velocities must be considered to calculate the wheel center velocities. Figure 5 shows the coordinate reference frame of the rover and the wheel, and the wheel center velocities generated by the combination of the rover surge u, sway v, and yaw r. Equation (4) calculates the longitudinal wheel center velocity, $u_{wc,n}$ and the lateral wheel centre velocity, $v_{wc,n}$, respectively.

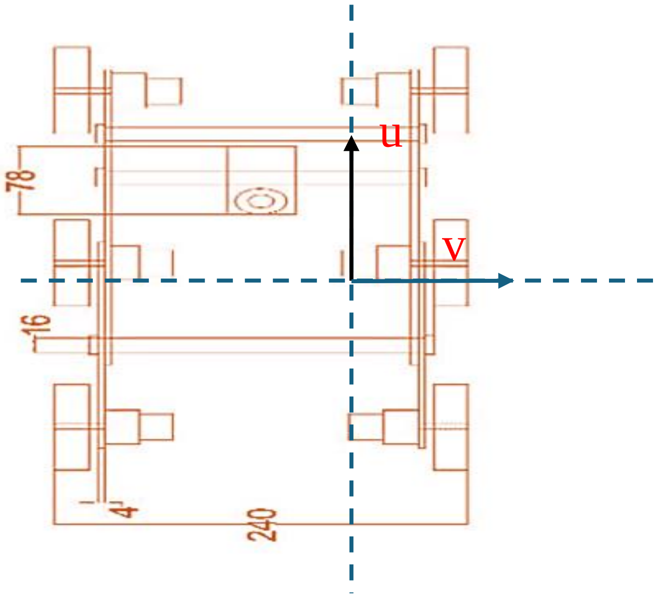

Fig. 5 Velocity components of the rover.

$$\begin{aligned} u_{wc,n} &= u - R_n.r.\cos(\gamma) \\ v_{wc,n} &= v + R_n.r.\sin(\gamma) \end{aligned} \quad (4)$$

From the rover geometry, this equation can be simplified using the relationships $X_n = \boldsymbol{R_n}.\sin(\boldsymbol{\gamma})$and $Y_n = \boldsymbol{R_n}.\cos(\boldsymbol{\gamma})$, giving the equations shown in Equation (5).

$$\begin{aligned} u_{wc,n} &= u - r.Y_n \\ v_{wc,n} &= v + r.X_n \end{aligned} \quad (5)$$

Slip

The longitudinal slip of the rover wheel is defined as the absolute difference between the longitudinal wheel center velocity and the tangential velocity resulting from the wheel's rotation. The resulting measurable slip Δv of the tire rotation velocity $r_{dyn}\omega_W$compared to the vehicle velocity v is due to a deformation part because of the elasticity of the tire treads and a relative movement part because of the partial gliding between the tire and the road, [7].

In Fig. 6, the slip is usually expressed as a relative value with reference to the larger rotational wheel velocity $v_{XW} = r_{dyn}\omega_W$ or longitudinal vehicle velocity v_{XT}.

Thus, the slip in the longitudinal direction is defined for braking

$$S_{x,b} = \frac{\Delta v_{XT}}{v_{XT}} = \frac{v_{XT} - v_{XW}}{v_{XT}} = \frac{v_{XT} - r_{dyn}\omega_W}{v_{XT}} \quad (6)$$

and for driving

$$S_{x,d} = \frac{\Delta v_{XT}}{v_{XW}} = \frac{v_{XW} - v_{XT}}{v_{XW}} = \frac{r_{dyn}\omega_W - v_{XT}}{r_{dyn}\omega_W} \quad (7)$$

$$S_x = \frac{|r_{dyn}\omega_W - v_{XT}|}{\max(r_{dyn}\omega_W - v_{XT})} \tag{8}$$

Where:
v_{XT} is the longitudinal tire traction velocity
v_{XW} the rotating velocity of the wheel

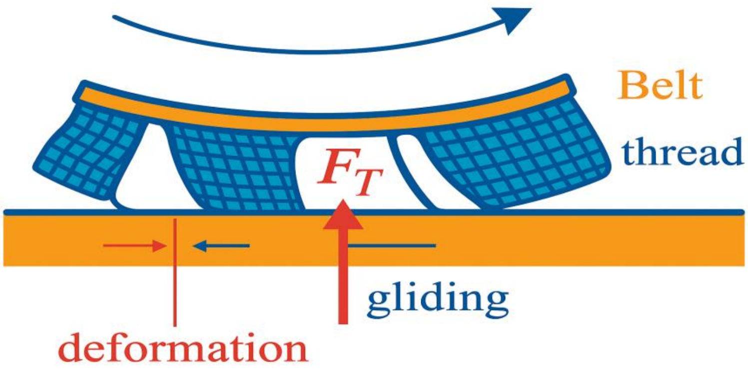

Fig. 6 Elastic deformation and partial gliding of a tire.

Friction Coefficient

The friction coefficients are defined as the ratio of the lateral or longitudinal forces to the vertical load through the wheel, as shown in Equation (6), [8]. This relationship allows the lateral and longitudinal forces to be calculated from the vertical forces. These vertical forces are calculated using the weight distribution

$$\mu_{XT} = \frac{F_{XT}}{F_{ZT}}$$
$$\mu_{ZT} = \frac{F_{YT}}{F_{ZT}} \tag{9}$$

The friction coefficients are functions of several variables, including slip, surface conditions, and sideslip angle. Several methods of modeling this behavior are discussed by Isermann, [7]. The friction coefficient $\mu(S_x)$ depends on the slip as shown in Fig.4. For small slips, it initially shows a linear behavior which is caused by the translatory deformation of the tire treads, increases with increasing slip to a maximal value μ_{max}at 10-30% slip where partial sticking and gliding in the contact patch appear, and then decreases to μ_{slip}until total slip S_x= 1 (100 %).

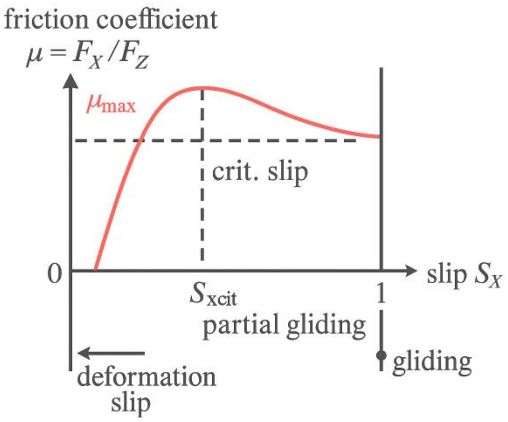

Fig. 7 Friction coefficient $\mu_X$in dependence on the tire slip.

Fig. 7, depicts μ-slip curves for different road surface conditions. It shows maximal values for dry asphalt, lower values for wet road. Different mathematical models for the longitudinal tire force have been obtained by approximation of the measured μ-slip curves. The $HSRI$ model [8] approximates μ_X by two straight lines

$$\begin{aligned} \mu_X &= c_{\mu 0} S_X & S_X &< S_{X,max} \\ \mu_X &= \mu_{X0} - c_{\mu 1} S_X & S_X &> S_{X,max} \end{aligned} \qquad \textbf{(10)}$$

where $S_{x,max}$ = $S_{x,Crit}$ is the slip for the maximum of $\mu X(S_x)$). The initial gradient

$$c_{\mu 0} = \left. \frac{d\mu_X}{dS_X} \right|_{S_X \to 0} \qquad \textbf{(10)}$$

is for dry and wet roads about the same [10]. The model according to [11] uses the approximation

$$\mu_X = c_1 \left(1 - e^{c_2 S_X}\right) - c_3 S_X. \qquad \textbf{(11)}$$

RESULTS AND DISCUSSION

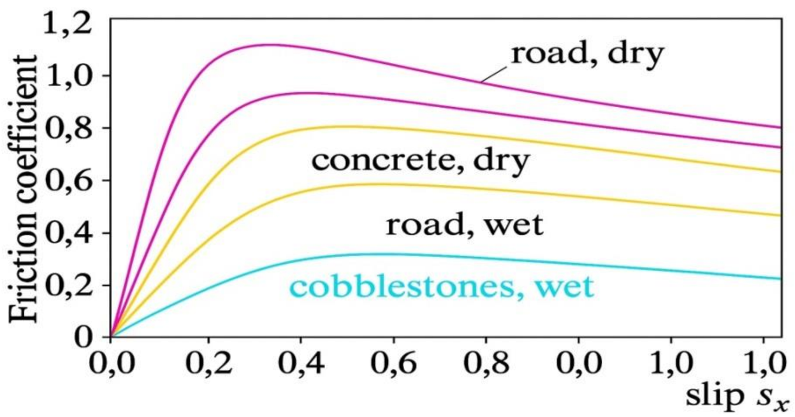

Fig. 8 Typical friction coefficients μ in dependence on slip S for different road surface conditions using python.

The relationship between slip and friction coefficient on various surfaces is depicted in Fig. 8. The data exhibits a typical non-linear pattern, with the friction coefficient rising with the slip ratio at first, peaking, and then progressively falling. Friction is strongest on a dry surface. These findings highlight how crucial road surface properties are to vehicle stability and braking effectiveness. losses in values and the proportion of aluminum oxide μ_{max}, the location of the maximum, and the value for total slip $S_x = 1$ are all determined by the coefficients c_1, c_2, and c_3. To get the same features, the simulation model uses the values derived from earlier experimental results as input data, [10 - 12].

The relation between friction coefficient and speed in different surfaces is shown in Fig. 9. A clean dry wheel on a clean dry surface may have a coefficient of friction as high as 0.35 or 35% at zero speed. This can drop to 0.25 in wet conditions, and very much lower if the rail is contaminated with lubricating substances such as ice, oil and leaves. However, the frictional coefficient between wheel and surfaces is not constant: due to "elastic slip". This falls as speed rises which is why wheel slips can occur at speed. The increase of speed tends to decrease the Friction coefficient. This can attribute the tires begin to dynamic friction comes into play. This type of friction is usually lower than static friction. When tires spin faster than the vehicle's speed, the friction force decreases.

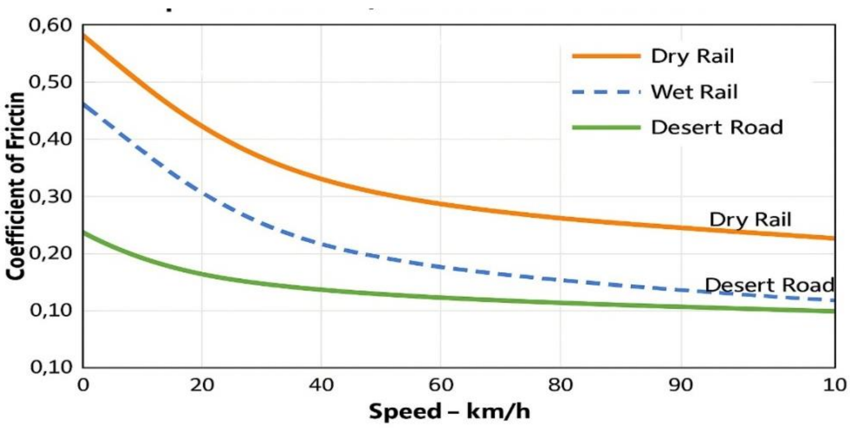

Fig. 9 the relationship between speed and friction coefficient using python.

CONCLUSIONS

1. The proposed friction model and control system improve the rover's performance and make it more reliable for such tasks.
2. The rover keeps good traction, save energy, and stay stable while moving.
3. Friction coefficient displayed by GT Car Wheels recorded the highest values compared to Low Friction Maroon Car Wheels.
4. The increase of speed tends to decrease the Friction coefficient. This is can attributed the tires begin to dynamic friction comes into play. This type of friction is usually lower than static friction. When tires spin faster than the vehicle's speed, the friction force decreases.

5. The simulation model makes it easy to know the Friction coefficient and contact slip.

REFERENCES

1. Wong J. Y. and Reece A. R., "Prediction of rigid wheel performance based on the analysis of soil–wheel stresses", Journal of Terramechanics, 4 (1), pp. 81 - 98, (1967).

2. Ishigami G., Nagatani K. and Yoshida K., "Terrain adaptive slip ratio for exploration rover on loose soil", Proceedings of the IEEE/RSJ International Conference on Intelligent Robots and Systems (IROS), pp. 3065 - 3070, (2007).

3. Zhang T., Wang D. and Yuan H., "Adaptive slip control for autonomous rovers using multi-sensor data fusion in deformable terrain", Sensors, 21 (5), p. 1825, (2021).

4. Zhang Q. and Wang J., "Physics-informed neural networks for wheel-soil interaction modeling in planetary exploration", Robotics and Autonomous Systems, 152, pp. 104 - 112, (2022).

5. Li H., Zhao Y. and Liu M., "A hybrid data-driven and physics-based model for real-time slip prediction in off-road environments", IEEE Transactions on Robotics, 39 (4), pp. 876 - 889, (2023).

6. Kumar S., Nair S. and Thomas J., "Friction testing in desert terrains for autonomous rover calibration. Journal of Field Robotics, 39 (2), pp. 215 - 229, (2022).

7. Kummer H. and Meyer W., "Verbesserter Kraftschluß zwischen Reifen und Fahrbahn", Automobiltechnische Zeitschrift – ATZ pp. 245 - 257 and pp. 382 - 386, (1967).

8. Dugoff H., Fancher P. and Segel L., "Tire performance characteristics affecting vehicle response to steering and braking control inputs", Highway Safety Research Institute, University of Michigan, Ann Arbor, National Bureau of Standards Control CST - 460, (1969).

9. Mitschke M. and Wallentowitz H., "Dynamik der Kraftfahrzeuge", 5th edn. Springer, Berlin, (2014).

10. Burckhardt M Fahrwerktechnik: Radschlupf-Regelsysteme, Vogel-Verlag, Würzburg, (1993).

11. Daiss A., "Beobachtung fahrdynamischer Zustände und Verbesserung einer ABS- und Fahrdynamikregelung", Diss. Universität Karlsruhe, Fortschr.-Ber. VDI Reihe 12, 283, VDI Verlag, Düsseldorf, (1996).

12. Halfmann C., Holzmann H., "Adaptive Modelle für die Kraftfahrzeugdynamik", VDI-Buch, Springer, Berlin, (2003).